

This is an Open Access document downloaded from ORCA, Cardiff University's institutional repository:<https://orca.cardiff.ac.uk/id/eprint/123155/>

This is the author's version of a work that was submitted to / accepted for publication.

Citation for final published version:

Didier, Joy, Miller, Amber D., Araujo, Derek, Aubin, François, Geach, Christopher, Johnson, Bradley, Korotkov, Andrei, Raach, Kate, Westbrook, Benjamin, Young, Karl, Aboobaker, Asad M., Ade, Peter, Baccigalupi, Carlo, Bao, Chaoyun, Chapman, Daniel, Dobbs, Matt, Grainger, Will, Hanany, Shaul, Helson, Kyle, Hillbrand, Seth, Hubmayr, Johannes, Jaffe, Andrew, Jones, Terry J., Klein, Jeff, Lee, Adrian, Limon, Michele, MacDermid, Kevin, Milligan, Michael, Pascale, Enzo, Reichborn-Kjennerud, Britt, Sagiv, Ilan, Tucker, Carole, Tucker, Gregory S. and Zilic, Kyle 2019. Intensity-coupled polarization in instruments with a continuously rotating half-wave plate. *Astrophysical Journal* 876 (1), 54. 10.3847/1538-4357/ab0f36

Publishers page: <http://dx.doi.org/10.3847/1538-4357/ab0f36>

Please note:





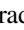
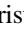
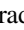


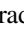


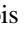
Changes made as a result of publishing processes such as copy-editing, formatting and page numbers may not be reflected in this version. For the definitive version of this publication, please refer to the published source. You are advised to consult the publisher's version if you wish to cite this paper.

This version is being made available in accordance with publisher policies. See <http://orca.cf.ac.uk/policies.html> for usage policies. Copyright and moral rights for publications made available in ORCA are retained by the copyright holders.





# Intensity-coupled Polarization in Instruments with a Continuously Rotating Half-wave Plate

Joy Didier<sup>1,2</sup> , Amber D. Miller<sup>1,2</sup>, Derek Araujo<sup>1</sup> , François Aubin<sup>3,4</sup> , Christopher Geach<sup>3</sup>, Bradley Johnson<sup>1</sup>, Andrei Korotkov<sup>5</sup>, Kate Raach<sup>3</sup>, Benjamin Westbrook<sup>6</sup>, Karl Young<sup>3</sup> , Asad M. Aboobaker<sup>3,7</sup>, Peter Ade<sup>8</sup> , Carlo Baccigalupi<sup>9</sup>, Chaoyun Bao<sup>3</sup>, Daniel Chapman<sup>1</sup>, Matt Dobbs<sup>4,10</sup>, Will Grainger<sup>11</sup>, Shaul Hanany<sup>3</sup> , Kyle Helson<sup>5,12</sup> , Seth Hillbrand<sup>1</sup>, Johannes Hubmayr<sup>13</sup>, Andrew Jaffe<sup>14</sup> , Terry J. Jones<sup>3</sup> , Jeff Klein<sup>3</sup>, Adrian Lee<sup>6</sup>, Michele Limon<sup>1,15</sup> , Kevin MacDermid<sup>4</sup>, Michael Milligan<sup>3</sup>, Enzo Pascale<sup>16</sup>, Britt Reichborn-Kjennerud<sup>1</sup>, Ilan Sagiv<sup>17</sup> , Carole Tucker<sup>8</sup>, Gregory S. Tucker<sup>5</sup> , and Kyle Zilic<sup>3</sup> 

<sup>1</sup> Physics Department, Columbia University, New York, NY 10027, USA; [didier.joy@gmail.com](mailto:didier.joy@gmail.com)

<sup>2</sup> Department of Physics and Astronomy, University of Southern California, Los Angeles, CA 90089, USA

<sup>3</sup> School of Physics and Astronomy and Minnesota Institute for Astrophysics, University of Minnesota/Twin Cities, Minneapolis, MN 55455, USA

<sup>4</sup> Department of Physics, McGill University, Montreal, Quebec, H3A 2T8, Canada

<sup>5</sup> Department of Physics, Brown University, Providence, RI 02912, USA

<sup>6</sup> Department of Physics, University of California, Berkeley, Berkeley, CA 94720, USA

<sup>7</sup> Jet Propulsion Laboratory, California Institute of Technology, Pasadena, CA 91109, USA

<sup>8</sup> School of Physics and Astronomy, Cardiff University, Cardiff, CF24 3AA, UK

<sup>9</sup> Astrophysics Sector, SISSA, Trieste, I-34014, Italy

<sup>10</sup> Canadian Institute for Advanced Research, Toronto, ON, M5G1Z8, Canada

<sup>11</sup> Rutherford Appleton Lab, Harwell Oxford, OX11 0QX, UK

<sup>12</sup> NASA Goddard Space Flight Center, Greenbelt, MD 20771, USA

<sup>13</sup> National Institute of Standards and Technology, Boulder, CO 80305, USA

<sup>14</sup> Department of Physics, Imperial College, London, SW7 2AZ, UK

<sup>15</sup> Department of Physics & Astronomy, University of Pennsylvania, Philadelphia, PA 19104, USA

<sup>16</sup> Department of Physics, La Sapienza Università di Roma, Roma, Italy

<sup>17</sup> Faculty of Physics, Weizmann Institute of Science, Rehovot 76100, Israel

Received 2018 February 27; revised 2019 March 9; accepted 2019 March 11; published 2019 May 3

## Abstract

We discuss a systematic effect associated with measuring polarization with a continuously rotating half-wave plate (HWP). The effect was identified with the data from the E and B Experiment, which was a balloon-borne instrument designed to measure the polarization of the cosmic microwave background (CMB) as well as that from Galactic dust. The data show polarization fractions larger than 10%, while less than 3% were expected from instrumental polarization. We give evidence that the excess polarization is due to detector nonlinearity in the presence of a continuously rotating HWP. The nonlinearity couples intensity signals to polarization. We develop a map-based method to remove the excess polarization. Applying this method to the 150 (250) GHz band data, we find that 81% (92%) of the excess polarization was removed. Characterization and mitigation of this effect are important for future experiments aiming to measure the CMB B-modes with a continuously rotating HWP.

*Key words:* balloons – cosmic background radiation – instrumentation: polarimeters – methods: data analysis – polarization – techniques: polarimetric

## 1. Introduction

Measurements of the cosmic microwave background (CMB) temperature and polarization provide a window into the physical mechanisms that govern the evolution of the universe. The E and B Experiment (EBEX) was a balloon-borne telescope designed to measure the polarization of the CMB while simultaneously measuring Galactic foreground emission. EBEX achieved polarimetry via a stationary wire-grid polarizer and a continuously rotating achromatic half-wave plate (HWP). The use of a continuously rotating HWP to modulate incident polarized radiation is a well-known polarimetric technique (see, e.g., Johnson et al. 2007; Kusaka et al. 2014). Continuous modulation of polarized signals is useful for mitigating systematic errors in two ways. It reduces the impact of low-frequency noise in the detectors by moving the polarization signal of interest to a higher frequency band, where the detector noise is primarily white. In addition, it enables the measurement of both the  $Q$  and  $U$  Stokes polarization parameters without differencing polarization-sensitive detectors. Differencing of signals among detector pairs requires

the responsivity and noise to be stable and well characterized, while mismatching of the detector beams is a source of systematic error, such as intensity-coupled-polarization (ICP) signals (Shimon et al. 2008; BICEP2 Collaboration et al. 2014), which is a common concern for experiments measuring B-modes, a curl pattern in the polarization of the CMB.

Intensity signals from the CMB and from foreground sources (including the atmosphere for ground-based experiments) can be orders of magnitude larger than CMB polarization signals. Even low levels of ICP add systematic bias to the polarization signal and can induce low-frequency noise if the intensity is time variable. A common source of ICP is instrumental polarization (IP). Here, IP is used in the traditional sense, referring to the conversion of intensity to polarization through differential transmission or reflection in optical elements. Another common source of ICP is beam and responsivity mismatch between detector pairs. Using a continuously rotating HWP can mitigate these sources of ICP: the IP is reduced because only optical elements sky side of the HWP primarily contribute to it, and the pair differencing effects are avoided

because polarization is measured without differencing detector pairs (Kusaka et al. 2014; Essinger-Hileman et al. 2016; Takakura et al. 2017).

The subject of this paper is the analysis of a new mechanism for creating ICP in EBEX, generated by detector nonlinearity in the presence of a rotation-synchronous signal generated by a HWP. A similar effect has been observed in Polarbear (Takakura et al. 2017), albeit with a different experimental setup: a warm, single sapphire plate HWP located directly behind a primary mirror. The scope of the two papers differ slightly: Takakura et al. (2017) provided a model linking detector parameters to nonlinearity, including the effect of detector time constant. This paper proposes a technique to mitigate the ICP, tested on both simulation and real data.

Understanding and mitigating this effect will be important for future CMB missions using a continuously rotating HWP. This paper describes the excess ICP observed in EBEX maps, outlines two possible sources for the excess polarization (IP and detector nonlinearity), uses data to distinguish between those two origins, and details the method we developed to characterize and remove the excess polarization. Because the magnitude of this ICP is correlated with a rotation-synchronous signal generated by the HWP, we also discuss sources of this rotation-synchronous signal.

This paper is organized as follows. In Section 2, we outline the data model of an experiment with a continuously rotating HWP. EBEX maps showing excess polarization are shown in Section 3. In Section 4, we provide two models for the physical origins of the ICP. In Section 5, we describe in detail the physical origins of the HWP synchronous signal. In Section 6, we characterize the ICP for each EBEX detector and show with this measurement that we can distinguish among various ICP mechanisms. In Section 7, we present the method we developed to remove the ICP and evaluate its performance on real and simulated data.

## 2. Data Model

The instrument is modeled by an achromatic HWP and a wire-grid analyzer (see Section 3.1). The HWP is rotating at a constant speed (in EBEX, the rotational frequency was 1.235 Hz), and we call the angle between the HWP extraordinary axis and the polarizing grid  $\gamma_t$ , where the subscript  $t$  is used to indicate time dependence. For a given Stokes vector  $\mathbf{S}_t^{\text{in}}$  incident on the receiver, the output Stokes vector  $\mathbf{S}_t^{\text{out}}$  at the detectors (integrated over the detector bandwidth) is

$$\begin{aligned} \mathbf{S}_t^{\text{out}} &= M_{\text{instr}} R(\psi_t) \mathbf{S}_t^{\text{in}} \\ &\simeq M_{\text{lp}} M_{\text{HWP}}(\gamma_t) R(\psi_t) \begin{pmatrix} I_t^{\text{in}} \\ Q_t^{\text{in}} \\ U_t^{\text{in}} \\ 0 \end{pmatrix}, \end{aligned} \quad (1)$$

$$\begin{aligned} M_{\text{instr}} &\simeq M_{\text{lp}} M_{\text{HWP}}(\gamma_t) \\ &= \frac{1}{2} \begin{pmatrix} 1 & \epsilon \cos(4\gamma_t - \Phi) & \epsilon \sin(4\gamma_t - \Phi) & 0 \\ 1 & \epsilon \cos(4\gamma_t - \Phi) & \epsilon \sin(4\gamma_t - \Phi) & 0 \\ 0 & 0 & 0 & 0 \\ 0 & 0 & 0 & 0 \end{pmatrix}, \end{aligned} \quad (2)$$

where  $M_{\text{lp}}$  and  $M_{\text{HWP}}(\gamma_t)$  are the ideal Mueller matrices of a linear polarizer and an HWP, respectively,  $\psi_t$  is the Galactic roll angle encoding the offset between the sky-fixed  $Q$  and  $U$  reference frame and the polarizing grid,  $R(\psi_t)$  is the Mueller rotation matrix,  $\epsilon$  is the HWP polarization modulation efficiency, and  $\Phi$  is the frequency-dependent phase delay introduced by the achromatic HWP (Matsumura 2006; Johnson et al. 2007). Details on the coordinates and the instrument and sky frames used throughout the paper are available in Appendix A. For simplicity, we do not write out  $\Phi$  or the modulation efficiency  $\epsilon$  in the paper. The detectors are only sensitive to the power  $I_t^{\text{out}}$  computed from Equation (1), and their time stream  $D_t$  is

$$\begin{aligned} D_t &= I_t^{\text{out}} \\ &= \frac{1}{2} (I_t^{\text{in}} + Q_t^{\text{in}} \cos(4\gamma_t - 2\psi_t) + U_t^{\text{in}} \sin(4\gamma_t - 2\psi_t)). \end{aligned} \quad (3)$$

We separate the incoming Stokes vector  $\mathbf{S}_t^{\text{in}}$  into the desired sky signals  $\mathbf{S}_t^{\text{sky}}$  and  $\mathbf{S}_t^{\text{instr}}$ , which correspond to spurious unpolarized and polarized signals from the instrument, giving

$$\begin{aligned} D_t &= \frac{1}{2} (I_t^{\text{sky}} + Q_t^{\text{sky}} \cos(4\gamma_t - 2\psi_t) + U_t^{\text{sky}} \sin(4\gamma_t - 2\psi_t)) \\ &\quad + A(\gamma_t) + n_t, \end{aligned} \quad (4)$$

where  $n_t$  is the detector noise and  $A(\gamma_t)$  groups spurious instrument signals  $\mathbf{S}_t^{\text{instr}}$  modulated by the HWP. The spurious modulation signal, called hereafter the HWP Synchronous Signal, or HWPSS, is modeled by

$$\begin{aligned} A(\gamma_t) &= \sum_{j=1}^{\infty} \underbrace{A_j \cos(j\gamma_t - 2\alpha_j)}_{\text{stationary}} \\ &\quad + \underbrace{A'_j I_t^{\text{sky}} \cos(j\gamma_t - 2\alpha'_j)}_{\text{scan modulated}}, \end{aligned} \quad (5)$$

where we have distinguished between stationary HWPSS from the instrument and scan-modulated HWPSS coupled to  $I_t^{\text{sky}}$ . All spurious effects are lumped into the  $A_j$ ,  $A'_j$ ,  $\alpha_j$ , and  $\alpha'_j$  parameters and are phenomenologically allowed to be present at all harmonics  $j$ .

The fourth harmonic amplitude terms ( $A_4$  and  $A'_4 I_t^{\text{sky}}$ ) represent instrumentally induced polarized power. This category includes:

1. The stationary signals represented by  $A_4$ , such as instrument polarized emissions and instrument unpolarized emissions polarized through IP. Instrument polarized and unpolarized emission are stationary in that they vary only with thermal variations in the instrument. As such, the  $A_4$  term, though it represents the largest polarization signal measured by the detectors (see Section 5), is separable from the sky polarization because it is constant over timescales on which the instrument is thermally stable.
2. Scan-modulated signals represented by  $A'_4 I_t^{\text{sky}}$ , which we call in this paper ICP. ICP includes two effects: IP acting on  $I_t^{\text{sky}}$ , which we label ICP<sup>IP</sup>, but also ICP arising from



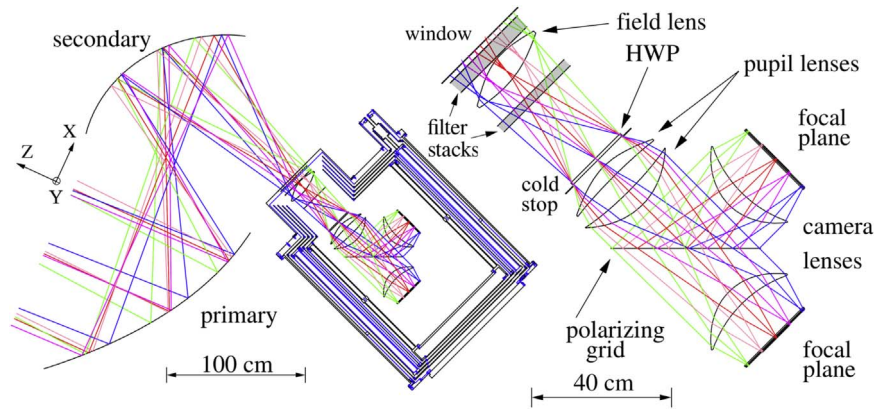


**Figure 1.** Ray tracing of the EBEX optical design consisting of two ambient temperature reflectors in a Gregorian configuration and a cryogenic receiver (left). Inside the receiver (right), cryogenically cooled polyethylene lenses formed a cold stop and provided diffraction-limited performance over a flat, telecentric,  $6.6^\circ$  field of view.

nonlinear detector response, which is the subject of this paper and which we label  $\text{ICP}^{\text{NL}}$ .

In the next section, we will show the ICP observed in EBEX maps. In Section 4, we describe in more detail the physical mechanisms generating  $\text{ICP}^{\text{IP}}$  and  $\text{ICP}^{\text{NL}}$ .

### 3. Intensity-coupled-polarization Observed in EBEX Maps

#### 3.1. The EBEX Instrument

A detailed description of the instrument is available in The EBEX Collaboration et al. (2018a, 2018b, 2018c). We provide here a summary relevant to the understanding of the origin of the ICP. The EBEX instrument was a balloon-borne telescope designed to measure the E- and B-mode polarization of the CMB while simultaneously measuring Galactic dust emission over the range  $30 < \ell < 1500$  of the angular power spectrum. To achieve sensitivity to both the CMB polarization signal and galactic foregrounds, EBEX had three bands centered on 150, 250, and 410 GHz.

The telescope optics comprised warm primary and secondary mirrors and a series of cold lenses and filters located inside a cryogenically cooled receiver (see Figure 1). The temperatures of the elements sky side of the HWP were 300 K for the mirrors and window, 77 K for the filter stack behind the window, and 4 K for the field lens and the filter stack behind it. EBEX achieved polarimetry via a stationary wire-grid polarizer and a 24 cm diameter continuously rotating achromatic HWP composed of a stack of five birefringent sapphire disks following a Pancharatnam design (Pancharatnam 1955). Incoming optical rays were focused onto each focal plane by a field lens and a series of pupil and camera lenses. The HWP was kept at 4 K and located at an aperture stop such that each detector beam covered the HWP. The field lens was located at an image of the focal plane. Each focal plane contained an array of transition-edge sensor (TES) bolometric detectors arranged into seven hexagonal wafers, with four 150 GHz wafers, two 250 GHz wafers, and one 410 GHz wafer per focal plane. EBEX operated 955 detectors during its science flight.

EBEX launched from McMurdo station, Antarctica, on 2012 December 29, circumnavigating the continent at an altitude of  $\sim 35$  km and landing 25 days later on 2013 January 23. We refer to data from this flight as EBEX2013. The cryogenic system that cooled the receiver was active for 11 days before cryogenics were depleted. Due to an error in thermal modeling (The EBEX Collaboration et al. 2018c), EBEX was unable to

point in azimuth, and as a result, EBEX scanned a  $5700 \text{ deg}^2$  strip of sky delimited by decl.  $-67.9^\circ$  and  $-38.9^\circ$ , corresponding to free rotations in azimuth at a constant elevation of  $54^\circ$ .

#### 3.2. EBEX Maps

We present here maps from EBEX2013 data and show that we observe ICP. To make the maps, we remove the stationary part of the HWPSS, calibrate and deconvolve the detector time constant, demodulate and filter the time streams to extract  $I$ ,  $Q$ , and  $U$ , and bin them into pixels. A detailed review of the time-stream processing is available in Didier (2016) and Araujo (2017), and the calibration is described in Aubin et al. (2016). Throughout the paper, we alternate between reconstructing the polarization in a frame rotation fixed with the Galactic coordinate system and a frame rotation fixed with the instrument (see definition in Appendix A). This is useful to separate polarization originating from the sky from polarization originating from the instrument, as each adds up coherently only in their respective frame orientations. When pointing in a given direction, the two frames are rotated from each other by the instrument Galactic roll angle  $\psi_i$  (see Equation (1)). Figure 2 shows the *Planck* and EBEX maps of the bright embedded cluster RCW 38 for Stokes  $I$  and the polarization power  $P$ , defined as  $P = \sqrt{Q^2 + U^2}$ . Polarization orientation is reconstructed in the instrument frame. *Planck* maps closest in frequency to the EBEX bands are first smoothed to the EBEX beam size. *Planck* time streams are then generated using the EBEX pointing and HWP angles, and those time streams are processed and binned into maps using the same pipeline as the EBEX2013 time streams. Excess polarization in the EBEX data is apparent for both 150 and 250 GHz maps. The  $I$  to  $P$  Pearson correlation coefficient and linear slope are given in Table 1. The correlation coefficient between  $I$  and  $P$  is 0.8 in EBEX2013 compared to less than 0.3 in *Planck*. This points to the excess polarization in EBEX2013 coming from ICP. The measured linear slopes of 11% (12%) for 150 (250) GHz correspond to a measurement of  $A_4'$  (from Equation (5)) averaged over detectors. These numbers are larger than the maximum anticipated IP of 2.7% as will be explained in Section 4.1.

We ascertain the existence of ICP by co-adding maps around cold and hot spots of the CMB intensity. The auto- and cross-intensity and polarization cosmological power spectra induce a correlation structure in the maps, which in turn generates

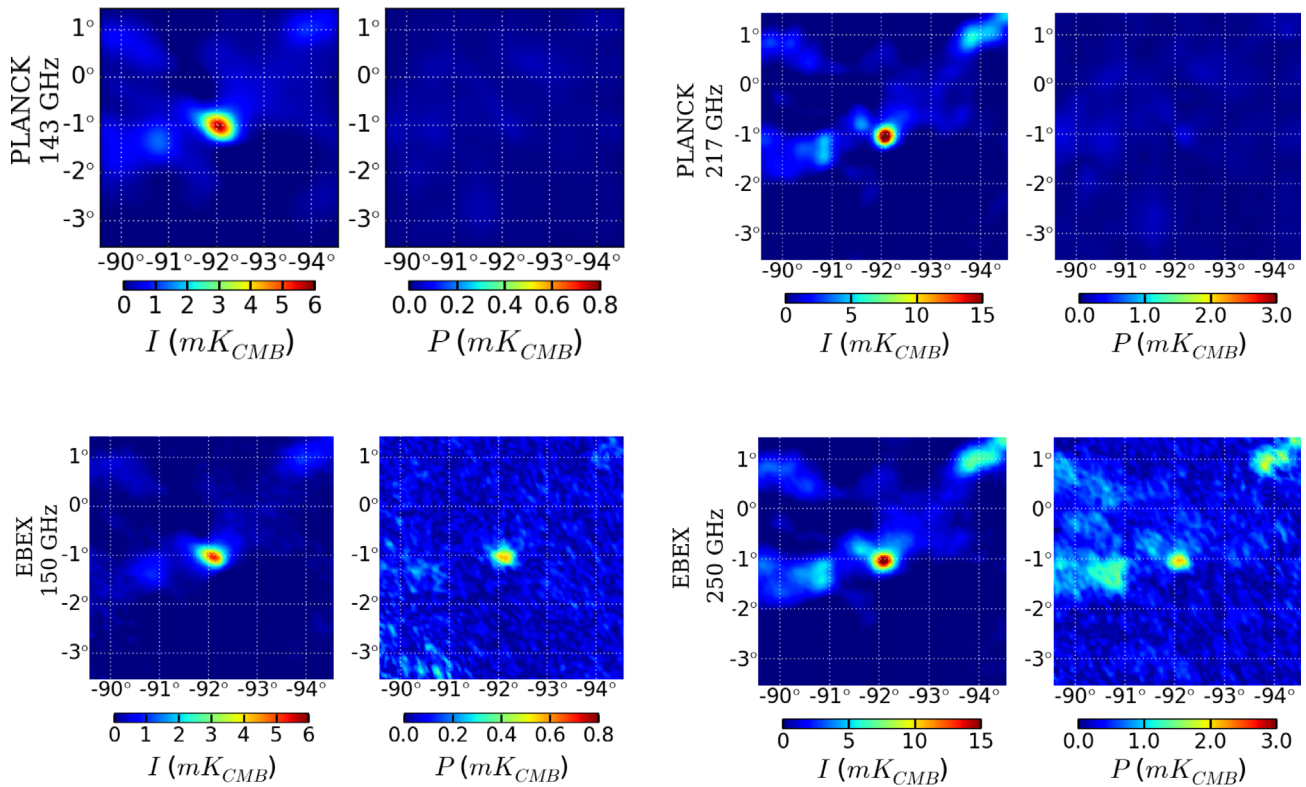


**Figure 2.** Comparison of RCW 38 maps in  $I$  and  $P$  among *Planck* at 143 GHz (top left), EBEX at 150 GHz (bottom left), *Planck* at 217 GHz (top right), and EBEX at 250 GHz (bottom right). The maps shown in Galactic coordinates co-add 332 (216) detectors at 150 (250) GHz. The polarization orientation is reconstructed in the instrument frame.

**Table 1**

Pearson Correlation and Linear Slope between  $I$  and  $P$  Using RCW 38 and Stacked CMB Maps

	RCW 38		CMB Stacked Spots	
	Correlation Coefficient	Linear Slope (%)	Correlation Coefficient	Linear Slope (%)
<i>Planck</i> 143 GHz	0.1	$0.2 \pm 0.1$	0.3	$0.0 \pm 0.1$
EBEX 150 GHz	0.8	$11 \pm 2$	0.8	$8 \pm 3$
<i>Planck</i> 217 GHz	0.3	$0.7 \pm 0.3$	0.2	$0.1 \pm 0.2$
EBEX 250 GHz	0.8	$12 \pm 3$	0.6	$16 \pm 6$

**Note.** The linear slope corresponds approximately to an average of  $A'_4$  across detectors. For RCW 38, only pixels with  $I$  greater than 2 (9) mK are used for 150 (250) GHz calculations. For CMB, only pixels with the absolute value of  $I$  greater than  $10 \mu\text{K}$  are used for calculations. The standard deviation on the slope indicated in the table is calculated by estimating the variance in the  $I$ ,  $Q$ , and  $U$  maps across pixels with no signal and propagating the error on the  $P/I$  ratio.

specific patterns around the hot and cold spot locations (Komatsu et al. 2011). Departures from these expected patterns can be due to systematic effects like ICP, which generate additional noncosmological correlations. We identify spot locations by examining the *Planck* CMB maps<sup>18</sup> (see Didier 2016). We smooth the EBEX  $I$ ,  $Q$ ,  $U$  maps to  $0.5^\circ$  ( $Q$ ,  $U$  are oriented in the instrument frame) and extract a square region of  $5^\circ \times 5^\circ$  around the spot extremum. The hot and cold

spots are stacked. Figures 3 and 4 show the resulting stacked spots from co-adding  $\sim 2000$  spots using the 150 and 250 GHz detectors, respectively. We show the stacked spots in  $I$  and also in polarization power  $P$  made from the  $Q$  and  $U$  stacked spots. In both EBEX and *Planck*, the CMB is visible in the co-added  $I$  maps. For polarization co-added in the instrument frame coupled to the EBEX scan strategy, we expect no CMB polarization power in the stacked spots, and none is observed in the *Planck*  $P$  data. In EBEX, polarization power is visible in the center of the stacked  $P$  map; this is the result of ICP. The correlation coefficient and linear slope between  $I$  and  $P$  are shown in Table 1, and the EBEX numbers are consistent between the RCW 38 and CMB stacked map measurements. In the next section, we describe in more detail the two mechanisms (IP and detector nonlinearity) responsible for ICP.

#### 4. Mechanisms for Intensity-coupled Polarization

We examine here two physical mechanisms responsible for ICP and trace the amplitude and polarization angle of each as a function of focal plane position. This provides a way to distinguish between them.

##### 4.1. Instrumental Polarization

Mirror and lenses sky side of the HWP are typical sources of IP in CMB instruments. Unpolarized radiation  $I_t^{\text{sky}}$  incident on the instrument will produce an ICP<sup>IP</sup> signal  $I_t^{\text{sky}} \varepsilon^{\text{IP}} \cos(4\gamma_t - 2\alpha^{\text{IP}})$  that has polarization fraction  $\varepsilon^{\text{IP}}$  and polarization angle  $\alpha^{\text{IP}}$ , where  $\varepsilon^{\text{IP}}$  and  $\alpha^{\text{IP}}$  are determined by the instrument configuration.

<sup>18</sup> [http://irsa.ipac.caltech.edu/data/Planck/release\\_2/all-sky-maps/cmbpreviews/COM\\_CMB\\_IQU-commander\\_1024\\_R2.02\\_full/index.html](http://irsa.ipac.caltech.edu/data/Planck/release_2/all-sky-maps/cmbpreviews/COM_CMB_IQU-commander_1024_R2.02_full/index.html)

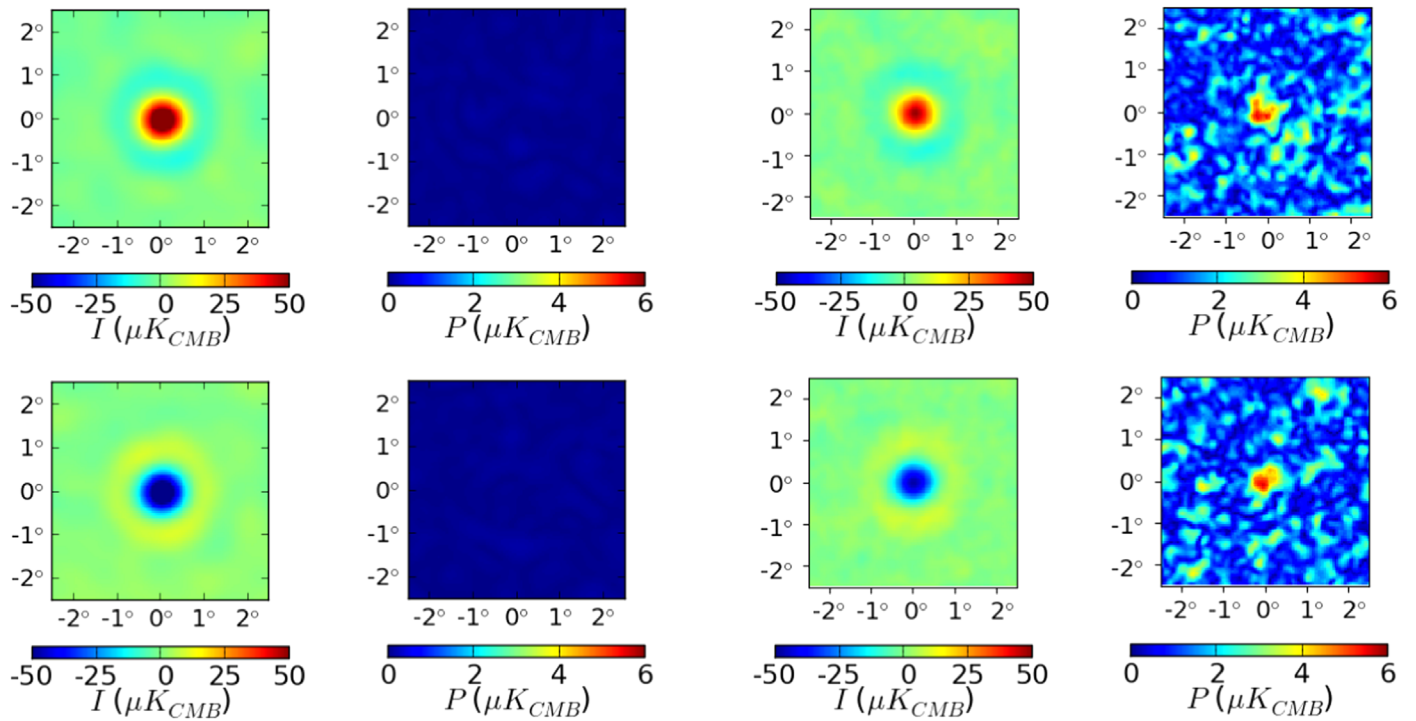


**Figure 3.** Co-added CMB hot and cold spots for *Planck* 143 GHz (left four) and EBEX 150 GHz (right four) in  $I$  and  $P$ . For each experiment, hot (cold) spots are shown on top (bottom) and co-add 2122 (2255) spots.

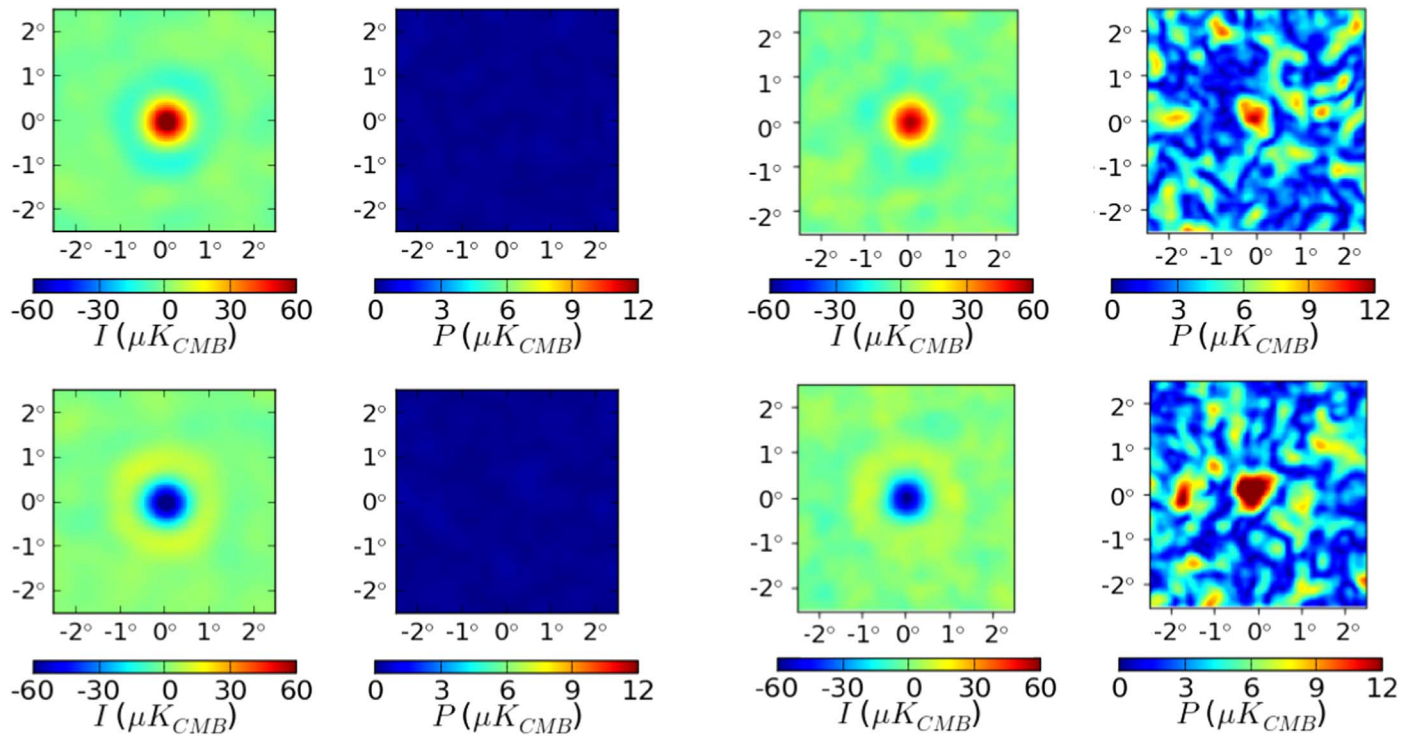


**Figure 4.** Co-added CMB hot and cold spots for *Planck* 217 GHz (left four) and EBEX 250 GHz (right four) in  $I$  and  $P$ . For each experiment, hot (cold) spots are shown on top (bottom) and co-add 1918 (2092) spots.

In EBEX, the optical design software Code V<sup>19</sup> shows that the main source of IP is the field lens, dominating the mirror IP by an order of magnitude at 150 and 250 GHz. Figure 1 shows

the location of and incident rays on the field lens, and Figure 5 gives the calculated IP of the final optical system including optical elements up to and including the field lens. The amount of IP from the field lens increases with distance  $d$  away from the lens center because of the increasing incident angles from

<sup>19</sup> <https://optics.synopsys.com/codev/>



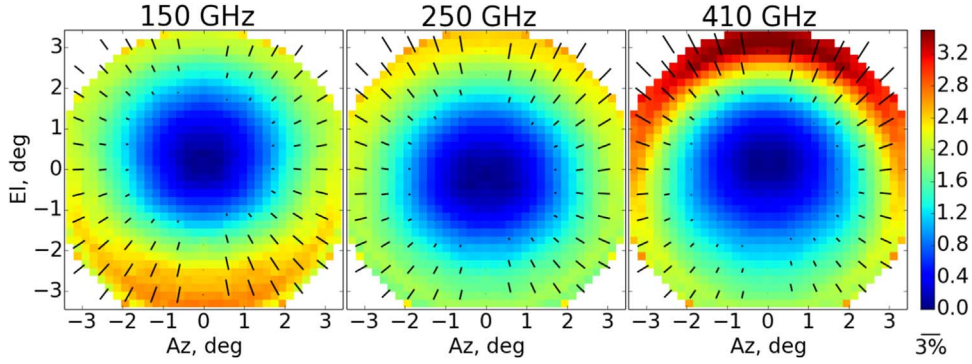


**Figure 5.** Magnitude and orientation of the calculated IP for the EBEX optics up to and including the field lens using Code V. Orientation is indicated by the polarization vectors (black bars). Both the color scale and the length of the polarization vectors give the IP magnitude.

the lens curvature. Unpolarized radiation  $I_t^{\text{sky}}$  incident on the lens will be polarized in the plane of incident light (see Appendix B for a general derivation). Over all rays hitting the field lens at a given location forming an angle  $\beta$  with the  $x$ -axis, the outgoing polarization will have a polarization angle  $\alpha^{\text{IP}} = \beta$ .

The EBEX field lens is located at an image of the focal plane such that the IP properties directly translate to the focal plane. Let the polar coordinates of a detector on the focal plane be its radial distance from the center  $r_{\text{det}}$  and its polar angle  $\rho_{\text{det}}$ . The detector illuminated by a ray hitting the field lens at radius  $d$  and angle  $\beta$  is the detector with coordinates  $r_{\text{det}} = d$  and  $\rho_{\text{det}} = \beta$ . Therefore, the ICP<sup>IP</sup> of each detector has a polarization angle  $\alpha^{\text{IP}}$  equal to the polar angle  $\rho_{\text{det}}$  of the detector position on the focal plane and a polarization fraction  $\varepsilon^{\text{IP}}$  that increases for a detector at the edge of the focal plane. Code V modeling for EBEX shows a maximum polarization fraction  $\varepsilon^{\text{IP}}$  of 2.7% at the edge of the focal plane for the 150 and 250 GHz frequency bands (The EBEX Collaboration et al. 2018b).

If IP is the dominant source of ICP in EBEX, we expect  $A_4'$  (from Equation (5)) to be of order  $\varepsilon^{\text{IP}} \sim 2.7\%$  given Code V predictions, and the ICP polarization angle  $\alpha_4'$  to be equal to the IP polarization angle  $\alpha^{\text{IP}}$ , which in EBEX is equal to the detector polar angle  $\rho_{\text{det}}$ . Future experiments wishing to mitigate ICP<sup>IP</sup> can diminish the magnitude of  $\varepsilon^{\text{IP}}$  by placing the HWP at the beginning of the optical chain: only optical elements sky side of the HWP primarily contribute to the total IP.

#### 4.2. Detector Nonlinearity

Another possible source of ICP is detector nonlinearity in the presence of an HWPSS with a fourth harmonic.

We derive the properties of the ICP<sup>NL</sup> using a simplified version of the data model in Equation (4) in which the incoming power on the detectors is composed solely of an unpolarized sky signal and a stationary fourth harmonic HWPSS parameterized by  $A_4$ :

$$D_t = I_t^{\text{sky}} + A_4 \cos(4\gamma_t - 2\alpha_4). \quad (6)$$

Let  $D_t$  vary over a range larger than the linear range of the detector response. For this derivation, we limit our nonlinearity model to second-order terms and ignore time-constant effects. We write the nonlinear detector response as

$$D_t^{\text{NL}} = f^{\text{NL}}(D_t) = D_t - KD_t^2, \quad (7)$$

where  $K$  has units of inverse power and characterizes the nonlinearity of the detector. For TES detectors tuned in the high-resistance regime of their superconducting transition, we can assume  $K > 0$ , as we show in Appendix C. We now rewrite the detector time stream as

$$\begin{aligned} D_t^{\text{NL}} &= f^{\text{NL}}(I_t^{\text{sky}} + A_4 \cos(4\gamma_t - 2\alpha_4)) \\ &= (1 - KI_t^{\text{sky}})I_t^{\text{sky}} \\ &\quad + 2A_4K I_t^{\text{sky}} \cos\left(4\gamma_t - 2\left(\alpha_4 + \frac{\pi}{2}\right)\right) \\ &\quad + A_4 \cos(4\gamma_t - 2\alpha_4) \\ &\quad - \frac{1}{2}KA_4^2 \cos(8\gamma_t - 4\alpha_4) - \frac{1}{2}KA_4^2. \end{aligned} \quad (8)$$

The nonlinear response has multiple effects:

1. it modifies  $I_t^{\text{sky}}$  by  $(1 - KI_t^{\text{sky}})$ ;
2. it creates an ICP<sup>NL</sup> signal  $2A_4KI_t^{\text{sky}} \cos\left(4\gamma_t - 2\left(\alpha_4 + \frac{\pi}{2}\right)\right)$ , with polarization fraction  $\varepsilon^{\text{NL}} = 2A_4K$  and polarization angle  $\alpha^{\text{NL}} = \alpha_4 + \frac{\pi}{2}$ ;
3. it creates higher harmonics in the HWPSS (in this second-order example, only an eighth harmonic), as well as modifies the DC level.

Our model does not include intrinsic sky polarization  $P_t^{\text{sky}}$ , but one can show similarly that nonlinearity modifies  $P_t^{\text{sky}}$  by  $(1 - 2KI_t^{\text{sky}})$ .

If nonlinearity is the dominant source of ICP in EBEX, we expect  $A_4'$  to be of order  $\varepsilon^{\text{NL}} = 2A_4K$ , and the ICP polarization angle  $\alpha_4'$  to be equal to the nonlinear model polarization angle  $\alpha^{\text{NL}}$ , which is offset from the stationary HWPSS fourth harmonic polarization angle  $\alpha_4$  by  $\frac{\pi}{2}$ . Note that because the polarization fraction of ICP<sup>NL</sup> is determined by the product of  $A_4$  and the detector nonlinearity  $K$ , future experiments wishing to minimize ICP<sup>NL</sup> can act on both the nonlinearity of the detectors ( $K$ ) and the magnitude of the stationary HWPSS fourth harmonic ( $A_4$ ), the latter by minimizing the polarized and unpolarized thermal emissions sky side of the HWP.

To determine the origin of the ICP observed in EBEX, we can measure the ICP polarization angle  $\alpha_4'$  and compare it to both  $\rho_{\text{det}}$  and to the stationary HWPSS polarization angle  $\alpha_4$ . In Section 6, we use the data to show that the ICP polarization angle  $\alpha_4'$  is consistent with a nonlinear origin of the signal and is not consistent with IP as its origin. We first determine the properties of the stationary HWPSS.

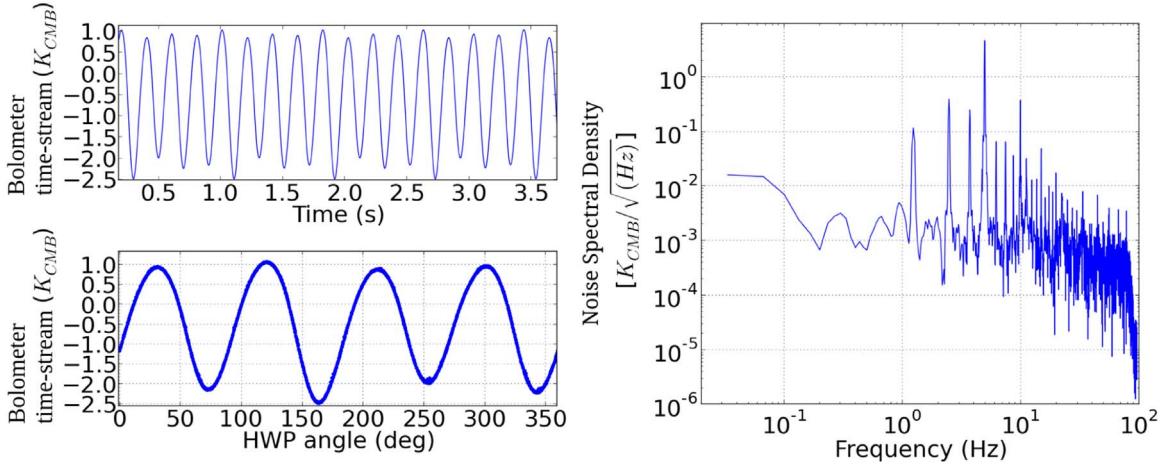


**Figure 6.** Left, top: plot of a calibrated detector time stream over 3.5 s of data prior to stationary HWPSS removal. The HWPSS has amplitude of 3.5 K and dominates the signal. Left, bottom: plot of the same detector time stream over 30 s vs. HWP angle, showing the HWPSS is synchronous with the HWP rotation. The fourth harmonic dominates the HWPSS. Right: noise spectral density of the same detector time stream.

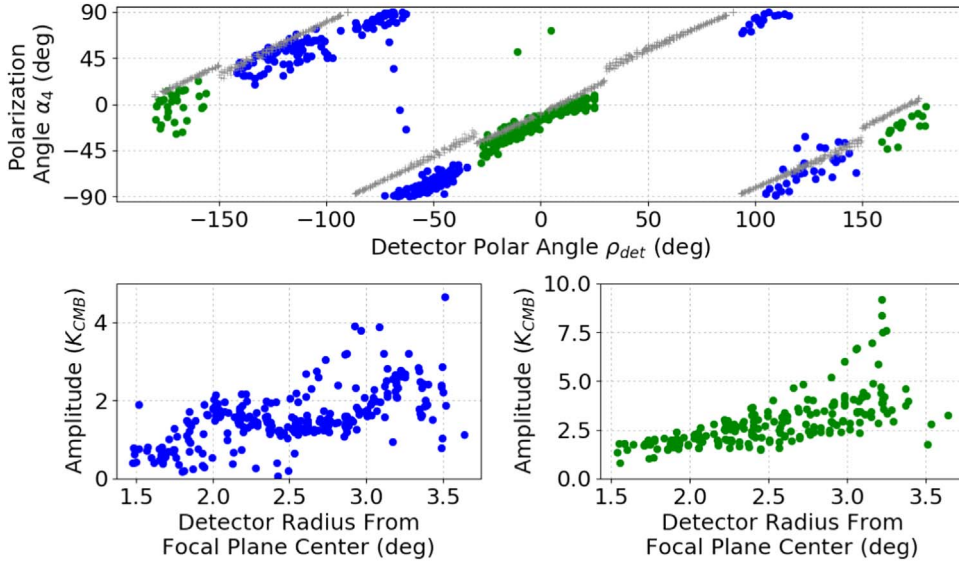


**Figure 7.** Top: polarization angle  $\alpha_4$  of the stationary HWPSS fourth harmonic for 150 (blue) and 250 (green) GHz detectors, plotted against the detector polar angle  $\rho_{det}$  on the focal plane, showing a strong 1:1 linear correlation between  $\alpha_4$  and  $\rho_{det}$ . The expected polarization angles from the Code V simulations are plotted in gray. We hypothesize that the difference between Code V simulations and the EBEX data is due to the polarized thermal emission of the primary mirror, which contributes to the stationary HWPSS fourth harmonic but is not modeled in Code V. Bottom: amplitude  $A_4$  of the stationary HWP fourth harmonic for 150 (left) and 250 (right) GHz detectors, plotted against the detector distance  $r_{det}$  from the focal plane center. Within each frequency band, the amplitude of the HWPSS increases with detector radius.

## 5. Stationary HWP Synchronous Signal

In Figure 6, we plot a detector time stream and the noise spectral density from EBEX, showing that an HWPSS dominates the detector time streams. The HWPSS has power at all harmonics of the HWP rotation up to the Nyquist frequency, with the fourth harmonic being the dominant harmonic by an order of magnitude. The stationary part of the HWPSS (coefficients  $A_j$ ,  $\alpha_j$  in Equation (5)) is fitted using a maximum likelihood estimator. We refer the reader to Didier (2016) and Araujo (2017) for a detailed review of the stationary HWPSS fitting and removal. The power in  $A_4$  comes from two sources sky side of the HWP: unpolarized power (thermal instrument emission, CMB monopole and atmosphere) getting polarized through IP, as well as polarized thermal emission from the instrument.

### 5.1. Unpolarized Thermal Emission Polarized through IP

In Section 4.1, we showed how IP acts on  $I_t^{\text{sky}}$  to produce  $ICP^{\text{IP}}$ . Similarly, IP will act on the power emitted by the instrument,  $I^{\text{instr}}$ , to produce a stationary polarized signal. As discussed earlier, in EBEX, because the dominant source of IP is the field lens located at an image of the focal plane, polarization signals generated by IP will exhibit a distinctive pattern as a function of focal plane position: the polarization angle will be equal to the polar angle of the detector, and the polarized power will increase with radial distance away from the focal plane center ( $A_4$  from IP is equal to  $I^{\text{instr}} \varepsilon^{\text{IP}}$ ). This is what we observe in the stationary HWPSS fourth harmonic, as shown in Figure 7 (top and bottom panels). These data indicate that field lens IP is a dominant source of the stationary HWPSS fourth harmonic. Its magnitude is estimated in Table 2 by



**Table 2**

HWPSS Fourth Harmonic Amplitude Predictions and Observations, Expressed as Power Incident on the Telescope

Frequency Band (GHz)	Estimated HWPSS	Predicted HWPSS	Observed HWPSS Size (fW)
	Size from Field Lens IP Using Flight Load (fW)	Size from Polarized Emission (fW)	
150	370	91	570
250	720	210	670
410	350	400	560

**Note.** The conversion from power to CMB temperature is 3.24, 4.54, and 16.1  $mK_{\text{CMB}}/fW$  at 150, 250, and 410 GHz. The two sources of HWPSS do not necessarily have the same polarization angle.

combining the thermal load on the detectors measured from flight with the IP predicted from Code V. We note that the load measured in flight was larger than what was predicted preflight. We hypothesize that the excess load comes from spillover onto warm, highly emissive surfaces around the mirrors, caused by diffraction around the aperture stop. The predicted and measured loads and a discussion of this effect are available in The EBEX Collaboration et al. (2018a). The excess load increased the amount of unpolarized light passing through the field lens and therefore the HWPSS.

### 5.2. Polarized Thermal Emission

We saw that contributions to  $A_4$  can come from IP (differential transmission) acting on instrument unpolarized thermal emission. Another possible contributor to  $A_4$  is instrument polarized thermal emission (differential emission). The dominant contribution of polarized thermal emission comes from the mirrors. The magnitude of this effect is estimated by combining the fraction of mirror thermal emission that is polarized ( $p^{\text{emission}}$ ) with the total radiative load from the mirrors, as discussed in The EBEX Collaboration et al. (2018a). The polarization fraction  $p^{\text{emission}}$  is a function of the angle of emission  $\theta$  with respect to normal incidence (Strozzi & McDonald 2000):

$$p^{\text{emission}} = \frac{\sin^2(\theta)}{1 + \cos^2(\theta)}. \quad (9)$$

The range of angles of emission that couple to our detectors is identical to the range of incidence angles for our optics. For the primary mirror, this range is from  $10^\circ$  to  $45^\circ$ , giving non-negligible polarization fractions. We average the polarization fraction across the beam for each of the mirrors, finding that the percentage of thermal emission that is polarized  $p^{\text{emission}}$  is 16% and 6.4% at the center of the focal plane for the primary and secondary mirrors, respectively. The polarization angle  $\alpha^{\text{emis}}$  of the polarized emission should be approximately uniform across the focal plane, with  $\alpha^{\text{emis}} \approx 0^\circ$ . We observe  $\alpha^{\text{emis}}$  to be nonzero in the top panel of Figure 7, indicating that polarized thermal emission is a subdominant contribution to the stationary HWPSS fourth harmonic.

### 5.3. Comparing Measurements to Model Predictions

Our estimate for the two contributions to the HWPSS (IP and polarized emission) is given in Table 2 along with the observed size of the HWPSS, all given in units of power incident on the telescope. We note that the HWPSS varies across detectors, and we only provide here average measurements and predictions. In particular, the two contributions will add differently for different locations across the focal plane given the varying polarization angles.

## 6. Single-detector Characterization of ICP

In this section, we present a general method for characterizing ICP coupling coefficients  $A_4'$  and  $\alpha_4'$  for each detector, independently of the ICP origin. The measurement of the coupling coefficients can inform the physical origin of the ICP and be used to remove the excess polarization.

In Equation (4), we showed that the power incident on a detector is the sum of the sky signal and the HWPSS, itself composed of a stationary term and a term modulated by the sky intensity  $I_t^{\text{sky}}$ . Having removed the stationary HWPSS term and now focusing on the dominant fourth harmonic, the detector time stream becomes

$$\begin{aligned} D_t^{\text{TOTAL}} &\sim \frac{1}{2}(I_t^{\text{sky}} + P_t^{\text{sky}} \cos(4\gamma_t - 2\psi_t - 2\alpha_t^{\text{sky}})) \\ &\quad + A_4' I_t^{\text{sky}} \cos(4\gamma_t - 2\alpha_4') + n_t \\ &\sim D_t^{\text{sky}} + D_t^{\text{ICP}} + n_t, \end{aligned} \quad (10)$$

where  $D_t^{\text{ICP}} = A_4' I_t^{\text{sky}} \cos(4\gamma_t - 2\alpha_4')$  stands for the ICP term,  $\alpha_t^{\text{sky}} = \frac{1}{2} \arctan\left(\frac{U_t^{\text{sky}}}{Q_t^{\text{sky}}}\right)$ ,  $\psi_t$  is the Galactic roll angle (see Section 2 for dropping  $\Phi$ ), and  $n_t$  is the noise. We note that the polarization of  $D_t^{\text{ICP}}$  originates in the instrument frame in contrast to the polarization of  $D_t^{\text{sky}}$ , which originates in the sky frame (hence its dependence on the Galactic roll angle  $\psi_t$ ).

To isolate and measure  $D^{\text{ICP}}$ , we make single-detector  $I$ ,  $Q$ , and  $U$  maps of  $D^{\text{TOTAL}}$  in the instrument frame. The value of each pixel  $p$  is

$$I_p = \frac{\sum_t w_t I_t^{\text{sky}}}{\sum_t w_t} + n_p^I = I_p^{\text{sky}} + n_p^I, \quad (11)$$

$$Q_p = Q_p^{\text{sky}} \frac{\sum_t w_t \cos(2\psi_t)}{\sum_t w_t} + I_p^{\text{sky}} A_4' \cos(2\alpha_4') + n_p^Q, \quad (12)$$

$$U_p = U_p^{\text{sky}} \frac{\sum_t w_t \sin(2\psi_t)}{\sum_t w_t} + I_p^{\text{sky}} A_4' \sin(2\alpha_4') + n_p^U, \quad (13)$$

where the summation is over all time samples  $t$  pertaining to a given pixel  $p$ ,  $w_t$  are the map-making weights, and  $n_p^{[I,Q,U]}$  is the pixel noise. Here we used the usual transformation  $Q_t^{\text{sky}} = P_t^{\text{sky}} \cos(2\alpha_t^{\text{sky}})$  and  $U_t^{\text{sky}} = P_t^{\text{sky}} \sin(2\alpha_t^{\text{sky}})$ . To measure the coupling parameters, an unpolarized source can be used ( $Q_p^{\text{sky}} = U_p^{\text{sky}} = 0$ ) or a polarized source can be sampled with varied Galactic roll such that  $\sum w_t \cos(2\psi_t)$  and  $\sum w_t \sin(2\psi_t)$  tend to zero. The coupling parameters for each detector are estimated from the maps using ensemble averages of  $I_p$ ,  $Q_p$ ,

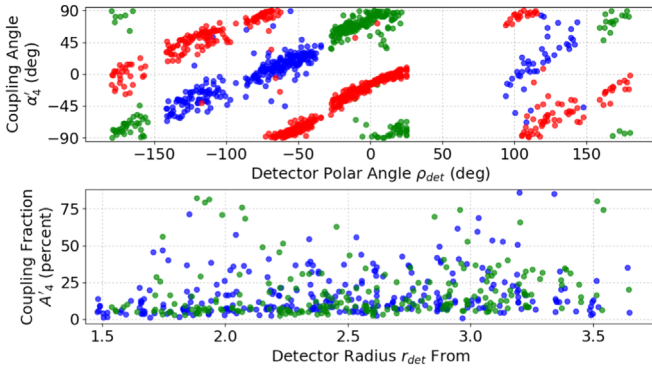


**Figure 8.** Top: measurement of the coupling angle  $\tilde{\alpha}'_4$  using the Galaxy for 150 (blue) and 250 (green) GHz detectors, plotted against the detector polar angle  $\rho_{\text{det}}$ . For reference, the HWPSS fourth harmonic polarization angle  $\alpha_4$  is also plotted (red). Bottom: measurement of the coupling fraction  $\tilde{A}'_4$  using the Galaxy for the 150 (blue) and 250 (green) GHz detectors, plotted against the detector radius from the focal plane center  $r_{\text{det}}$ .

and  $U_p$ :

$$\tilde{A}'_4 = \frac{\sqrt{\langle Q_p \rangle^2 + \langle U_p \rangle^2}}{\langle I_p \rangle}, \quad (14)$$

$$\tilde{\alpha}'_4 = \frac{1}{2} \arctan \left( \frac{\langle U_p \rangle}{\langle Q_p \rangle} \right), \quad (15)$$

where the tilde denotes the measured quantity. For EBEX, the three possible sources are the CMB, RCW 38, and the Galactic plane. EBEX does not have enough sensitivity to measure the CMB with single detectors. RCW 38 is sampled with enough signal to noise but poor coverage. This leaves the Galaxy, which has intrinsic polarization. For an extended source like the Galaxy, summing all of the pixels within the source will increase the signal to noise and the sampling of  $\psi_l$ . Using simulations, we estimate the error on the coupling parameters coming from the partial Galactic roll coverage to be 1.7% for  $\tilde{A}'_4$  and  $3^\circ$  for  $\tilde{\alpha}'_4$  for the EBEX scan strategy.

For each detector, we produce  $I$ ,  $Q$ , and  $U$  maps of the Galactic plane in the instrument orientation, with Healpix NSIDE 256 (Górski et al. 2005). We define as valid the pixels located within  $\pm 3^\circ$  of the Galaxy and with Stokes  $I$  value greater than or equal to 3 (15) mK for the 150 (250) GHz detectors. We calculate for each detector the ensemble average  $\langle I \rangle$ ,  $\langle Q \rangle$ , and  $\langle U \rangle$  values by averaging all valid pixels. Using those values and Equation (14), we estimate  $\tilde{A}'_4$  and  $\tilde{\alpha}'_4$  for each detector, and plot the results in Figure 8. We observe that the coupling angle  $\tilde{\alpha}'_4$  varies linearly with the detector polar angle  $\rho_{\text{det}}$  and that the coupling fractions  $\tilde{A}'_4$  are spread over a wide range with a mode of 7% and a median absolute deviation of 5.7%. These  $\tilde{A}'_4$  values are roughly consistent with the RCW 38 and CMB linear slopes reported in Table 1, which correspond to weighted averages of  $A'_4$  over the detectors used in those maps.

### 6.1. Origin of ICP in EBEX

Comparing the measured polarization angle  $\tilde{\alpha}'_4$  to the stationary HWPSS polarization angle  $\alpha_4$  is a good way to determine the origin of the ICP. For ICP<sup>IP</sup>, the two angles should have the same phase, given that both the ICP and the

stationary HWPSS originate from the IP from the field lens. In the ICP<sup>NL</sup> case, the two angles should be offset by  $\pi/2$  as we showed in Section 4.2. Furthermore, the coupling fraction  $A'_4$  for the IP model should be of order 2.7% as predicted by Code V, whereas in the nonlinear model  $A'_4$  is proportional to the HWPSS fourth harmonic amplitude  $A_4$  and the amount of nonlinearity  $K$ . Finally, a second-order nonlinear response gives rise to an eighth harmonic in the HWPSS, and a more complex nonlinear response will give rise to a multitude of higher harmonics in the HWPSS. The presence of those harmonics can be checked in the HWPSS data. We note that higher harmonics can also come from temperature and thickness variations in the HWP and are not necessarily a consequence of nonlinearity in the detectors.

Figure 8 (top panel) shows the measured coupling angle  $\tilde{\alpha}'_4$  as a function of the detector polar angle  $\rho_{\text{det}}$ , as well as the stationary HWPSS fourth harmonic polarization angle  $\alpha_4$ . The coupling angle  $\tilde{\alpha}'_4$  varies linearly with the detector polar angle  $\rho_{\text{det}}$ , which is expected in both the IP model and the nonlinear model. The two sets of angles are offset by  $\pi/2$ , indicating that the nonlinear effect is likely to be the dominant source of ICP. Additional support for the model where ICP<sup>NL</sup> is dominant comes from the bottom panel of Figure 8, which shows that the coupling fractions  $\tilde{A}'_4$  are spread over a wide range and on average larger than the maximum  $\varepsilon^{\text{IP}}$  of 2.7% calculated by the Code V simulation. Finally, a strong eighth harmonic and a multitude of higher harmonics are observed in the EBEX HWPSS as can be seen in Figure 6.

To summarize, the observed properties of the HWPSS and the ICP point to the following model. Unpolarized instrument emissions are polarized through differential transmission by the field lens and cause a fourth harmonic in the HWPSS with a large amplitude and a polarization angle  $\alpha_4$  that varies linearly with the detector polar angle  $\rho_{\text{det}}$ . The magnitude of the HWPSS induces a nonlinear response in the detectors, which is synchronous with the HWPSS. The nonlinear response couples unpolarized sky signal to the polarization signal bandwidth. The polarization angle  $\alpha'_4$  of the coupling is offset by  $\pi/2$  from the HWPSS fourth harmonic polarization angle. The nonlinear response explains why the observed coupling fractions  $\tilde{A}'_4$  are larger than those predicted by optical simulations in Code V and contributes to higher harmonics in the HWPSS. In the next section, we use the measured coupling parameters to remove the spurious polarization in the time domain.

## 7. Removal of the ICP

Having measured the coupling parameters, we now produce corrected time streams  $D_i^C$  for each detector

$$D_i^C = D_i^{\text{TOTAL}} - \tilde{D}_i^{\text{ICP}}, \quad (16)$$

where  $D_i^{\text{TOTAL}}$  is the measured detector time stream including the ICP (see Equation (10)) and  $\tilde{D}_i^{\text{ICP}} = \tilde{A}'_4 I_i^{\text{sky}} \cos(4\gamma_i - 2\tilde{\alpha}'_4)$  is the measured ICP.

To produce  $\tilde{D}_i^{\text{ICP}}$ , we use for each detector the measured parameters  $\tilde{A}'_4$  and  $\tilde{\alpha}'_4$  plotted in Figure 8. Alternatively, in the case of ICP<sup>NL</sup>, we can compute  $\tilde{\alpha}'_4$  from the stationary HWPSS fourth harmonic polarization angle:  $\tilde{\alpha}'_4 = \alpha_4 + \pi/2$ . The two methods produce similar results. In the former method, the contribution of the detector time constant to the ICP, which was ignored in this paper, can be included. However, if the HWPSS

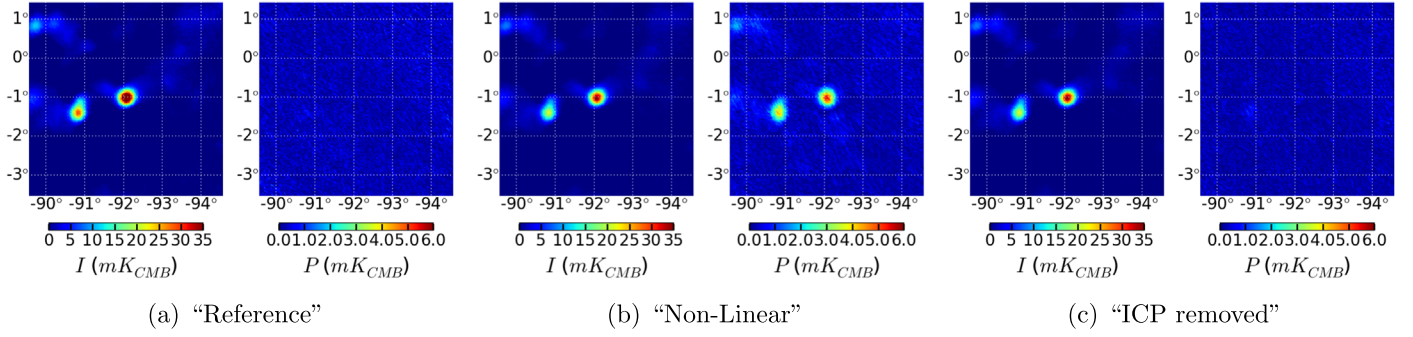


**Figure 9.** Simulations of RCW 38 maps in intensity and polarization power  $P$  for three simulated data sets: “reference” (left), nonlinear (middle), and “ICP removed” (right). The maps shown in Galactic coordinates co-add 216 detectors. The polarization orientation is reconstructed in the instrument frame.

angle  $\alpha_4$  varies over time, for example, because the mirror temperature varies and the contribution of the polarized emission becomes significant,  $\alpha'_4$  will vary accordingly, and this will be reflected by using  $\tilde{\alpha}'_4 = \alpha_4 + \pi/2$ .  $I_t^{\text{sky}}$  is generated using the detector pointing and a reference  $I$  map. The reference  $I$  map is constructed from the *Planck* Sky Model for simulations and from the *Planck* component maps for EBEX data, in each case integrated over the EBEX frequency bandwidth. Finally, we make EBEX  $Q^{\text{sky}}$  and  $U^{\text{sky}}$  maps using the corrected time streams  $D_t^C$  with the same pipeline that was presented in Section 3. In the following subsections, we present RCW 38 maps and CMB stacked spots generated from the cleaned time streams. We present results for both simulations and EBEX2013 data.

### 7.1. Simulations

We use simulations to evaluate the ICP removal method. Though the method removes the ICP from any source, our simulations focus on ICP<sup>NL</sup> because it is the dominant source in EBEX. We compare maps made from three data sets:

1. A “reference” data set, obtained from scanning an input sky with detectors that have a linear response (hence no ICP<sup>NL</sup>).
2. A “nonlinear” data set, obtained from scanning the same input sky with detectors that have a nonlinear response.
3. An “ICP-removed” data set, obtained from scanning the same input sky with detectors that have a nonlinear response and then applying the ICP removal technique described earlier.

We simulate detector time streams as follows:

$$D_t^{\text{SIM}} = f^{\text{NL}} \left[ \frac{1}{2} (I_t^{\text{sky}} + Q_t^{\text{sky}} \cos(4\gamma_t - 2\psi_t)) + U_t^{\text{sky}} \sin(4\gamma_t - 2\psi_t) + \sum_{j=1}^{j=4} A_j \cos(j\gamma_t - 2\alpha_j) + n_t \right]. \quad (17)$$

$I_t^{\text{sky}}$ ,  $Q_t^{\text{sky}}$ , and  $U_t^{\text{sky}}$  are generated by scanning input maps with the EBEX scan strategy. The input maps come from the *Planck* Sky Model integrated over the EBEX bandwidth and smoothed to the EBEX beam size. We present here the simulations for the 250 GHz detectors. The nonlinear response  $f^{\text{NL}}$  is set to identity to simulate the reference data set. For the nonlinear and ICP-removed data sets, we use the following polynomial

**Table 3**  
Pearson Correlation and Linear Slope between  $I$  and  $P$  using RCW 38 and Stacked CMB Spots

	RCW 38		CMB Stacked Spots	
	Correlation Coefficient	Linear Slope (%)	Correlation Coefficient	Linear Slope (%)
Simulation “reference”	0.0	$0.0 \pm 0.5$	0.2	$0 \pm 2$
Simulation “nonlinear”	0.9	$13 \pm 1$	1.0	$17 \pm 2$
Simulation “ICP removed”	0.1	$0.2 \pm 0.5$	0.3	$0 \pm 2$

**Note.** The linear slope corresponds approximately to the average of the coupling fractions  $A_4$  across detectors. For RCW 38, only pixels with  $I$  greater than 9 mK are used for calculations. For CMB, only pixels with  $I$  greater than 10  $\mu$ K are used for calculations. The difference in linear slopes between RCW 38 and the CMB stacked spots is similar to what is observed in EBEX data and likely comes from the difference in detector coverage.

estimated from EBEX data (Araujo 2017):

$$f_{\text{NL}}(D_t) = D_t - 0.04D_t^2 + 0.001D_t^3, \quad (18)$$

where the second and third coefficients are in units of  $K_{\text{CMB}}^{-1}$  and  $K_{\text{CMB}}^{-2}$ , respectively. The stationary HWPSS is simulated using only the largest physically motivated harmonics 1, 2, and 4, though after the nonlinear response is applied multiple higher harmonics are present. The HWP coefficients  $A_j$  and  $\alpha_j$  are sampled from EBEX2013 data ensuring the simulated HWPSS has similar amplitude and focal plane dependence as the EBEX HWPSS. EBEX-level white noise  $n_t$  is added except when otherwise noted.

We measure the coupling parameters of each detector in the simulated nonlinear data set using the map-based method with the Galaxy as a source described in Section 6. With the measured coupling parameters, we subtract the ICP from the time streams using Equation (16) to produce the ICP-removed data set, and finally we make maps of the cleaned time stream. Note that the removal method only removes ICP; it does not correct for other nonlinear effects such as the compression of  $I_t^{\text{sky}}$  and  $P_t^{\text{sky}}$  described in Section 4.2. We present in Figures 9–11 maps of RCW 38 and the stacked CMB spots comparing the three simulated data sets. Table 3 gives quantitative correlations between  $I$  and  $P$  for the simulated data sets. To calculate how much ICP is removed, we take the ratio of the difference of polarized power in the nonlinear and



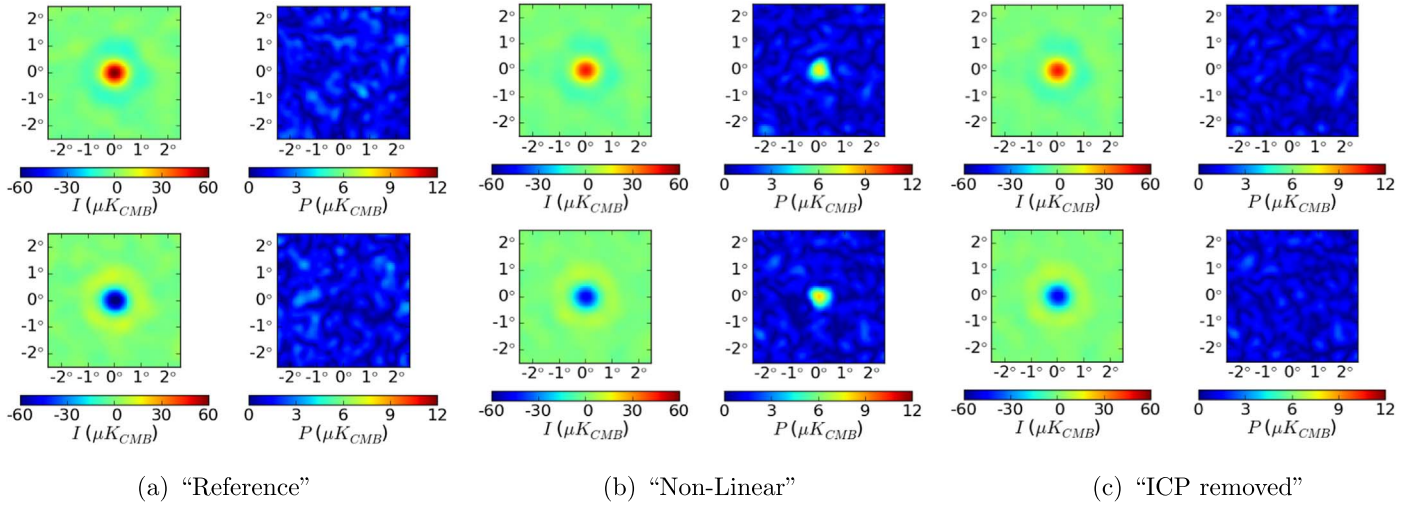


**Figure 10.** Simulations of CMB stacked spots in intensity and polarization power  $P$  for three simulated data sets: “reference” (left), “nonlinear” (middle), and “ICP removed” (right). The polarization orientation is reconstructed in the instrument frame. 95% of the 17% ICP is removed in the cleaned data set (right).

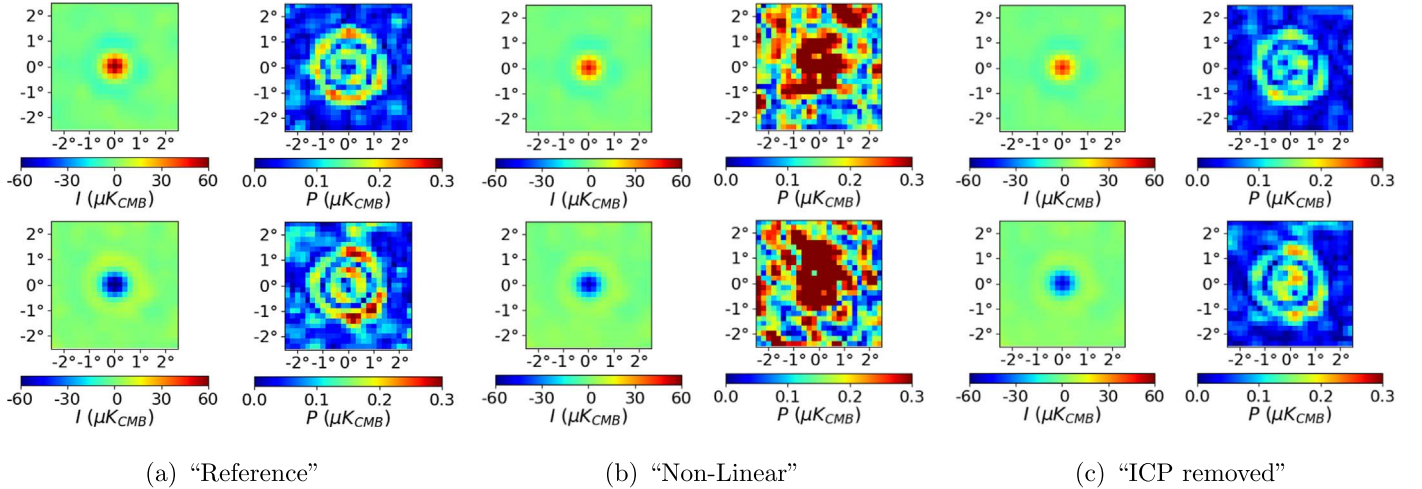


**Figure 11.** Simulations of CMB stacked spots in intensity and polarization power  $P$  for three simulated data sets: “reference” (left), “nonlinear” (middle), and “ICP removed” (right). The polarization orientation is reconstructed in the sky frame. Note that the color scale in polarization is different from the previous stacked spots presented, and that these simulations are noiseless. These noiseless maps were produced early in the analysis and have a larger pixel size than the other stacked spots presented in the paper.

ICP-removed data set to the polarized power in the nonlinear data set. We note this is a lower limit as it does not take into account the noise, which will bias the measurement.

**RCW 38:** Figure 9 shows the RCW 38 maps in intensity  $I$  and polarization power  $P$  for each of the three simulated data sets. A 13% coupling fraction is apparent from the simulated nonlinear data set in the middle panel, which is consistent with the 12% coupling measured in EBEX data (see linear slope in Table 1). The removal of the coupling is evident in the ICP-removed data set (right panel): 98% of the ICP has been removed.

**CMB Stacked Spots in the Instrument Frame:** Figure 10 shows the CMB stacked spots constructed from the three simulated data sets. The polarization orientation is co-added in the instrument frame. The nonlinear time streams (middle) produce a coupling fraction of 17% that is visible in the center of the  $P$  stacked spots. The coupling coefficients produced by the nonlinear simulation are in agreement with those measured

in EBEX data (see linear slope in Table 1). In the ICP-removed data set, 95% of the ICP has been removed.

**CMB Stacked Spots in the Sky Frame:** we plot in Figure 11 the stacked spots in the sky frame for the three simulated data sets. When stacking CMB spots in the sky frame, E-modes are apparent as rings of polarization power surrounding the cold and hot  $I$  spots. For this analysis, we used noiseless simulations because adding the EBEX2013 level of noise would have entirely obscured the polarization structure apparent in Figure 11(a). The 17% ICP completely obscures the E-modes in the nonlinear data set. In the ICP-removed data set, 99% of the ICP is removed, and the standard deviation between the input and recovered E-modes is  $0.01 \mu\text{K}$ .

## 7.2. EBEX2013

The ICP removal procedure is applied to EBEX2013 data, for both 150 and 250 GHz detectors. The Galaxy is used to measure coupling coefficients, which are then used to produce

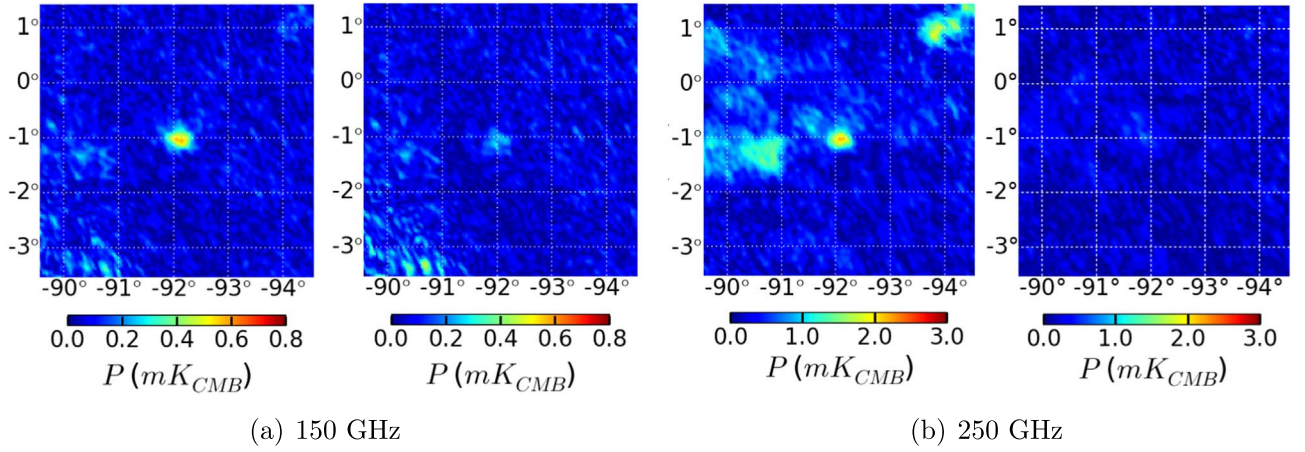


**Figure 12.** Comparison of RCW 38 maps in polarization power  $P$  before (left) and after (right) ICP removal for the 150 GHz (a) and 250 GHz (b) EBEX detectors. The polarization orientation is reconstructed in the instrument frame.

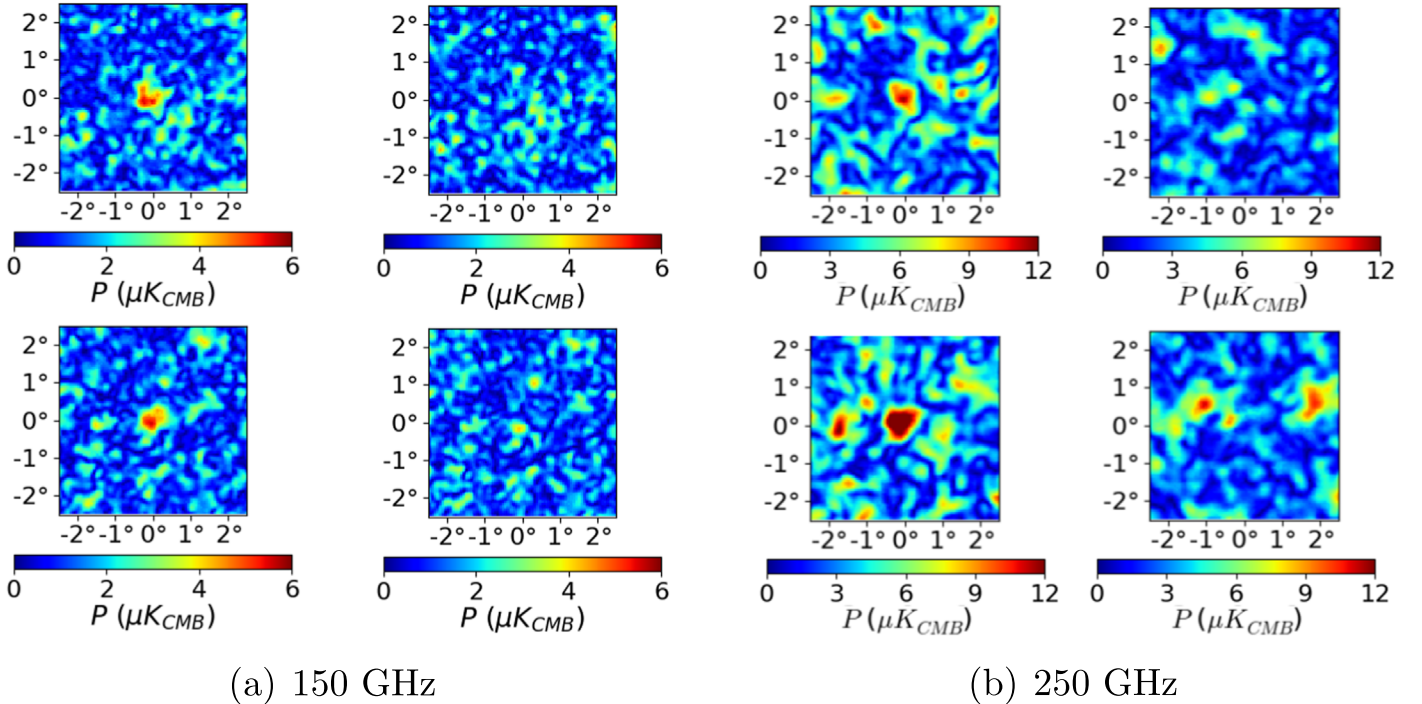


**Figure 13.** Comparison of CMB stacked spots in polarization power  $P$  before and after ICP removal for 150 GHz (left four) and 250 GHz (right four) EBEX detectors. Within each frequency band, the maps are shown before (left) and after (right) excess polarization removal. Hot and cold spot are shown in the top and bottom panels, respectively. The polarization orientation is reconstructed in the instrument frame.

**Table 4**

Pearson Correlation and Linear Slope between  $I$  and  $P$  after Excess Polarization Removal

	RCW 38		CMB Stacked Spots	
	Correlation Coefficient	Linear Slope (%)	Correlation Coefficient	Linear Slope (%)
EBEX 150 GHz	0.8	$11 \pm 2$	0.8	$8 \pm 3$
EBEX 150 GHz with ICP removed	0.4	$3 \pm 1$	0.2	$2 \pm 3$
EBEX 250 GHz	0.8	$12 \pm 3$	0.6	$16 \pm 6$
EBEX 250 GHz with ICP removed	0.5	$0 \pm 1$	0.1	$1 \pm 5$

**Note.** For ease of comparison, the preremoval numbers are copied over from Table 1. The linear slope corresponds approximately to  $A'_4$  averaged over detectors.

time streams with the ICP removed. We present RCW 38 maps generated before and after removal in Figure 12 and CMB stacked spots in Figure 13. Table 4 summarizes the ICP Pearson correlation and coupling coefficients in each frequency band before and after removal of the excess polarization. For RCW 38, 67% (98%) of the ICP is removed at 150 (250) GHz. In the stacked spots, 81% (92%) of the excess polarization is removed.

### 7.3. Discussion and Summary

Continuously rotating HWPs are increasingly used in CMB instruments because they reduce the ICP originating from detector differencing and because they mitigate low-frequency noise, enabling observations on large angular scales, which are otherwise limited by atmospheric turbulence. Considering the ICP alone, the



HWP should be the first element in the optical path in order to modulate only incident polarized sky signals. With the EBEX instrument, which had a 1.5 m entrance aperture, it was not practical for the HWP to be the first element in the optical path. We placed it behind the field lens, heat-sunk to a temperature of 4 K, to reduce optical load on the detectors. We anticipated ICP<sup>IP</sup> of up to 2.7%. The data showed an ICP larger than 10%. We found that the relatively large HWPSS induced a nonlinear detector response, which in turn caused significant conversion of intensity signals to polarization, ICP<sup>NL</sup>.

We developed and applied an ICP removal method to the EBEX2013 data, using the Galaxy to measure coupling parameters and assessing the quality of the removal on RCW 38 maps and CMB stacked spots. We showed that for the EBEX2013 data, 81% (92%) of the ICP was removed from the CMB at 150 (250) GHz using this technique. The removal of the ICP performs better at 250 GHz compared to 150 GHz. We think this is due to the 150 GHz detectors having an elliptical beam that is not taken into account during calibration or when using a reference map to measure the coupling parameters and subtract the excess polarization (only a symmetrical fit to the beam is used). This would also explain why the ICP removal works better on the CMB stacked spots smoothed to 0.5 compared to RCW 38 maps, which vary on smaller scales. We note that the CMB stacked spots are a good test of the quality of the removal as it uses a separate data set (CMB) than that used to compute the coupling parameters (Galaxy).

The method we presented removes ICP regardless of its source. However, if the detectors have a nonlinear response, other effects are present in addition to ICP<sup>NL</sup>, such as a change in  $I_t^{\text{sky}}$  and  $P_t^{\text{sky}}$ , an effect that can be seen in the simulations (comparing  $I$  in the reference and nonlinear plots in Figures 9 and 10) given that we do not recalibrate the nonlinear data set. These effects are not corrected by the ICP removal method. Our method, as is the method presented by Takakura et al. (2017), does not correct the nonlinearity of the detectors and does not correct the distortion induced on incident sky  $Q$  and  $U$  Stokes signals. The level of these distortion needs to be assessed separately, particularly for experiments targeting higher precision polarimetry. Alternatively, nonlinearity should be avoided by reducing the range of incoming signals (in particular the HWPSS) or by using detectors with operating parameters that ensure a linear response over a larger dynamic range of incident signals.

J.D. acknowledges the NASA NESSF fellowship NNX11 AL15H. Support for the development and flight of the EBEX instrument was provided by NASA grants NNX12 AD50G, NNX 13AE49G, NNX08AG40G, and NNG05GE62G, and by NSF grants AST-0705134 and ANT-0944513. We acknowledge support from the Italian INFN INDARK Initiative. P.A. and C. T. acknowledge the Science & Technology Facilities Council for its continued support of the underpinning technology for filter and waveplate development. We also acknowledge support by the Canada Space Agency, the Canada Research Chairs Program, the Natural Sciences and Engineering Research Council of Canada, the Canadian Institute for Advanced Research, the Minnesota Supercomputing Institute, the National Energy Research Scientific Computing Center, the Minnesota and Rhode Island Space Grant Consortia, our collaborating institutions, and Sigma Xi the Scientific Research Society. C.B. acknowledges support from the RADIOFOREGROUNDS grant of the European Union's Horizon 2020 research and innovation program

(COMPET-05-2015, grant agreement No. 687312) and the INDARK INFN Initiative.

B.R.-K. acknowledges an NSF Post-doctoral Fellowship AST-1102774 and a NASA Graduate Student Research Fellowship. K.R. and K.Z. acknowledge support by the Minnesota Space Grant Consortium. K.H. acknowledges NASA NSTRF fellowship NNX11AN35H. We very much thank Danny Ball and his colleagues at the Columbia Scientific Balloon Facility for their dedicated support of the EBEX program. We thank the referee for his detailed comments, which helped improve the paper.

## Appendix A Coordinates

For the celestial reference frame, we adopt the *Wilkinson Microwave Anisotropy Probe* conventions (Komatsu et al. 2011): the polarization that is parallel to the Galactic meridian is  $Q > 0$  and  $U = 0$ , and the polarization that is rotated by 45° from east to west (clockwise, as seen by an observer on Earth looking up at the sky) has  $Q = 0$  and  $U > 0$ . In the instrument frame, positive  $Q$  corresponds to linear polarization along the  $x$ -axis and positive  $U$  corresponds to a polarization of 45° between the  $+x$  and  $+y$  directions. The axes are labeled in Figure 1. When pointing in a given direction, the two frames are rotated from each other by the instrument Galactic roll angle  $\psi_t$  (see Equation (1)).

## Appendix B Effect of a Di-attenuator on Unpolarized Light

The field lens acts as a di-attenuator and polarizes light because of differential transmittance between the in-plane and out-of-plane incidence. The Mueller matrix of a di-attenuator with in-plane direction forming an angle  $\delta$  with the  $x$ -axis is

$$G(\delta) = \frac{1}{2} R(-\delta) \begin{pmatrix} \eta & \varepsilon & 0 & 0 \\ \varepsilon & \eta & 0 & 0 \\ 0 & 0 & \sqrt{\eta^2 - \varepsilon^2} & 0 \\ 0 & 0 & 0 & \sqrt{\eta^2 - \varepsilon^2} \end{pmatrix} R(\delta),$$

where  $R(\delta)$  is the Mueller rotation matrix,  $\eta \sim 2$  is the sum of the transmittances along the two perpendicular axis, and  $\varepsilon \sim 0$  is the difference between the transmittances of the two axes. The amount of IP is characterized by  $\varepsilon$ , which we call  $\varepsilon^{\text{IP}}$  in the text. Note that  $\varepsilon^{\text{IP}}$  increases as the angle of incident light increases, producing more IP at the edge of the field lens than in the center. To calculate the effect of the field lens on incoming unpolarized light  $I$ , the instrument Mueller matrix is modified to include  $G(\delta)$ :

$$M_{\text{instr}} = M_{\text{Ip}} M_{\text{hwp}}(\gamma_t) G(\delta). \quad (19)$$

Using Equations (19) and (3), this results in the following detector time stream:

$$\begin{aligned} S_t^{\text{IP}} &= M_{\text{instr}} \begin{pmatrix} I^{\text{instr}} \\ 0 \\ 0 \\ 0 \end{pmatrix}, \\ D_t^{\text{IP}} &= I_t^{\text{IP}} \\ &= \frac{1}{2} I^{\text{instr}} (\eta + \varepsilon^{\text{IP}} \cos(4\gamma_t - 2\delta)). \end{aligned} \quad (20)$$



### Appendix C Nonlinear Response of a TES Bolometer

In the EBEX detector readout (Aubin 2012; MacDermid 2014), the change in the current  $i$  coming from a change in the power  $\delta P$  incident on the detector can be expanded into a series about the equilibrium point  $i_0$ :

$$i(\delta P) - i_0 = \frac{di}{dP}\delta P + \frac{1}{2}\frac{d^2i}{dP^2}\delta P^2 + \dots \quad (21)$$

$$= a\delta P + b\delta P^2 + \dots \quad (22)$$

We limit our nonlinearity model to second-order terms and ignore time-constant effects. Let us show that  $a$  and  $b$  have opposite signs, which will justify our subsequent choice of nonlinear function. The current  $i$  is a function of the bias voltage  $V$  and the detector resistance  $R(T)$ :

$$i = \frac{V}{R(T)}, \quad (23)$$

such that the current  $i$  can be expressed as

$$i(\delta P) - i_0 = -\frac{V}{R_0^2}\frac{dR}{dT}\frac{dT}{dP}\delta P + \left(\frac{V}{R_0^3}\left[\frac{dR}{dT}\right]^2 - \frac{1}{2}\frac{V}{R_0^2}\frac{d^2R}{dT^2}\right)\left[\frac{dT}{dP}\right]^2\delta P^2 \quad (24)$$

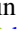




$$= a\delta P + b\delta P^2, \quad (25)$$

where  $R_0$  is the detector resistance at the equilibrium point. We assume the thermal response to incoming power is linear.  $a$  is negative because  $R$  increases with increasing temperature  $T$  and the temperature increases with increasing power  $P$ , and  $b$  is positive because in TES detectors,  $\frac{d^2R}{dT^2}$  is negative high in the transition (during the EBEX flight,  $R_0$  was at 65% to 85% of its overbiased resistance  $R_N$ ). Dividing by the responsivity  $a$ , we can write the nonlinear detector response as

$$f^{\text{NL}}(\delta P) = \delta P - K\delta P^2, \quad (26)$$

where  $K > 0$ .

### ORCID iDs

Joy Didier  <https://orcid.org/0000-0003-4151-9450>  
 Derek Araujo  <https://orcid.org/0000-0003-0527-2948>  
 François Aubin  <https://orcid.org/0000-0002-8241-4156>  
 Karl Young  <https://orcid.org/0000-0002-1337-6088>  
 Peter Ade  <https://orcid.org/0000-0002-5127-0401>  
 Shaul Hanany  <https://orcid.org/0000-0002-8702-6291>  
 Kyle Helson  <https://orcid.org/0000-0001-9238-4918>  
 Andrew Jaffe  <https://orcid.org/0000-0003-2086-1759>  
 Terry J. Jones  <https://orcid.org/0000-0002-8716-6980>  
 Michele Limon  <https://orcid.org/0000-0002-5900-2698>  
 Ilan Sagiv  <https://orcid.org/0000-0001-8377-3153>  
 Gregory S. Tucker  <https://orcid.org/0000-0002-6954-6947>  
 Kyle Zilic  <https://orcid.org/0000-0003-1971-7151>

### References

- Araujo, D. 2017, PhD thesis, Columbia Univ.  
 Aubin, F. 2012, PhD thesis, McGill Univ.  
 Aubin, F., Aboobaker, A. M., Ade, P., et al. 2016, in Proc. 14th Marcel Grossman Conf., Meeting on Recent Developments in Theoretical and Experimental General Relativity, Astrophysics, and Relativistic Field Theories, ed. M. Bianchi, R. T. Jantzen, & R. Ruffini (Hackensack, NJ: World Scientific), 2084  
 BICEP2 Collaboration, Ade, P. A. R., Aikin, R. W., et al. 2014, *PhRvL*, **112**, 241101  
 Didier, J. 2016, PhD thesis, Columbia Univ.  
 Essinger-Hileman, T., Kusaka, A., Appel, J. W., et al. 2016, *RSci*, **87**, 094503  
 Górski, K. M., Hivon, E., Banday, A. J., et al. 2005, *ApJ*, **622**, 759  
 Johnson, B., Collins, J., Abroe, M., et al. 2007, *ApJ*, **665**, 42  
 Komatsu, E., Smith, K. M., Dunkley, J., et al. 2011, *ApJS*, **192**, 18  
 Kusaka, A., Essinger-Hileman, T., Appel, J. W., et al. 2014, *RSci*, **85**, 024501  
 MacDermid, K. 2014, PhD thesis, McGill Univ.  
 Matsumura, T. 2006, PhD thesis, Univ. Minnesota  
 Pancharatnam, S. 1955, *InMS*, **41**, 137  
 Shimon, M., Keating, B., Ponthieu, N., & Hivon, E. 2008, *PhRvD*, **77**, 083003  
 Strozzi, D. J., & McDonald, K. T. 2000, arXiv:physics/0005024  
 Takakura, S., Aguilar, M., Akiba, Y., et al. 2017, *JCAP*, **5**, 8  
 The EBEX Collaboration, Aboobaker, A. M., Ade, P., et al. 2018a, *ApJS*, **239**, 7  
 The EBEX Collaboration, Aboobaker, A. M., Ade, P., et al. 2018b, *ApJS*, **239**, 8  
 The EBEX Collaboration, Aboobaker, A. M., Ade, P., et al. 2018c, *ApJS*, **239**, 9